Observation of Megagauss-Field Topology Changes due to Magnetic Reconnection in Laser-Produced Plasmas

C. K. Li, F. H. Séguin, J. A. Frenje, J. R. Rygg, and R. D. Petrasso
Plasma Science and Fusion Center, Massachusetts Institute of Technology, Cambridge, Massachusetts 02139, USA

R. P. J. Town and O. L. Landen
Lawrence Livermore National Laboratory, Livermore, California 94550 USA

J. P. Knauer and V. A. Smalyuk
Laboratory for Laser Energetics, University of Rochester, Rochester, New York 14623, USA
(Received 30 April 2007; published 2 August 2007)

The spatial structure and temporal evolution of megagauss magnetic fields generated by interactions of up to 4 laser beams with matter were studied with an innovative, time-gated proton radiography method that produces images of unprecedented clarity because it uses an isotropic, truly monoenergetic backlighter (14.7-MeV protons from D^3He nuclear fusion reactions). Quantitative field maps reveal precisely and directly, for the first time, changes in the magnetic topology due to reconnection in a high-energy-density plasma ($n_e \sim 10^{20}$–10^{22} cm^{-3}, $T_e \sim 1$ keV).

DOI: 10.1103/PhysRevLett.99.055001 PACS numbers: 52.38.Fz, 52.35.Vd, 52.50.Jm, 52.70.Nc

The interaction and reconnection of magnetic (B) fields in plasmas are important fundamental processes [1] with implications for a wide range of basic sciences, including astrophysics [2], space physics [3], and laboratory physics [4–6]. In the frontier field of high-energy-density (HED) physics (pressures >1 Mbar) [7,8], the generation, evolution, and reconnection of B fields due to laser-plasma interactions [9,10] takes place in an extreme physical regime. High plasma densities ($> \sim 10^{20}$ cm^{-3}), high temperatures (~1 keV), intense B fields [~1 megagauss (MG)], and high ratios of thermal pressure to magnetic pressure ($\beta \gg 1$) distinguish this novel regime from tenuous plasmas, of order 10^{14} cm^{-3} or (usually much) lower, that are the more traditional venue of reconnection experiments [1,4]. Here we describe experiments involving the first direct observation of field reconnection in the HED regime, where plasma flow is dominated by hydrodynamics and is not strongly affected by fields, even though MG fields are present. The results have fundamental implications for basic reconnection physics in all regimes. In addition, the methodology is quite general and is applicable to a wide class of basic physics experiments. These include HED physics experiments in which precise, time-resolved field measurements are a necessity [7,8], and experiments involving strongly coupled, warm dense matter (WDM) [11] where the energy loss of monoenergetic, charged particles can be related to the dynamic interaction between the transiting particles and the WDM [12].

Megagauss B fields are generated in a hot, high-density plasma by illuminating a solid material with a high-power laser beam [9,10,13–15]. The laser heats the material, forming an expanding, hemispherical plasma bubble with an intense, toroidal B field on its surface. The dominant source for field generation is noncollinear electron density and temperature gradients ($\nabla n_e \times \nabla T_e$) [13–17]. While the bubble is hot and expanding, the dominant mechanism for field transport is convection [$\nabla \times (\mathbf{v} \times \mathbf{B})$, where $\mathbf{v}$ is the plasma fluid velocity]; at later times, when the laser is off and the cooling plasma becomes more resistive, field diffusion dominates convective transport [i.e., $\nabla \times (D_m \nabla \times \mathbf{B})$, where D_m is the magnetic diffusion coefficient].

Recent single-laser-beam experiments [18] at the OMEGA laser facility [19] have demonstrated that the hemispherical bubble radius grows linearly while the laser is on, and then continues to expand after the laser is off. It was shown that the plasma density (n_e) was $\sim 10^{20}$–10^{22} cm^{-3}, the temperature (T_e) was ~1 keV, and the B fields were ~1 MG [13,18]. It follows that the ratio of thermal pressure to field pressure was $\beta \gg 1$, indicating that plasma motion and field behavior in these bubbles were dominated by plasma fluid dynamics rather than fields.

When nonoverlapping laser beams impinge on a material, each generates an expanding, conductive plasma bubble with an associated B field. If the beams are close enough, the bubbles eventually encounter each other with B fields of opposing sign and reconnection will occur. The experiments described here were designed for mapping the spatial structure and time evolution of fields around multiple bubbles, from when lasers were turned on to well after lasers were off, allowing the whole processes of field generation and bubble interaction to be observed. In contrast to other recently reported two-bubble interaction experiments [15] that postulate reconnection, but for which field maps were not measured, we directly measured B fields and the topological changes due to reconnection. OMEGA laser beams with a wavelength of 0.351 μm were used in a 1-ns long, square pulse. The energy in each beam was ~500 J, with a spot diameter of 800 μm (containing 95% of beam energy [20]), and a resultant laser

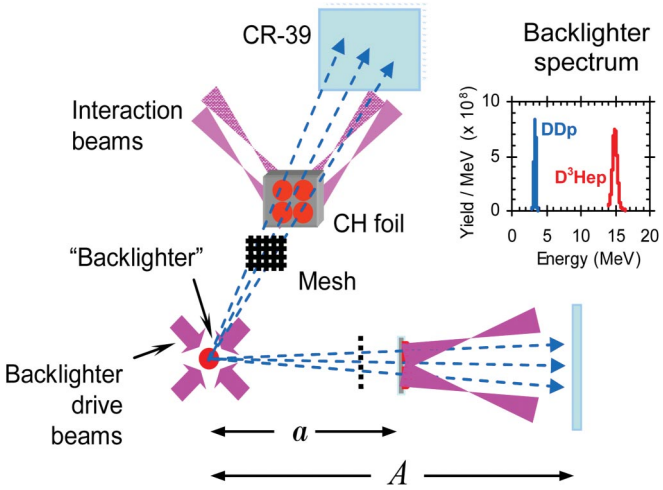

FIG. 1 (color). Experimental setup. The mesh was 60-μm–thick Ni with 75-μm holes separated by 75-μm wires. Distances were $a = 1.5$ cm, $A = 30$ cm, and backlighter-to-mesh = 1.3 cm. The measured backlighter spectrum is typical (separate images can be made with both types of protons, but only D^3He protons are used here).

intensity of $\sim 10^{14}$ W cm^{-2}. Two or four of these (interaction) beams were incident on a 5-μm-thick, plastic (CH) foil.

The novel arrangement used for imaging the spatial structure and temporal evolution of the fields is shown in Fig. 1. The laser-illuminated foil was backlit by protons at the discrete energy of 14.7 MeV produced in fusion reactions ($D + {}^3He \rightarrow \alpha + p$) in an imploded, $D\,{}^3He$-filled, glass-shell capsule driven by 20 OMEGA laser beams [13,18]. The duration of proton emission from the backlighter was ~150 ps, and the timing of the interaction laser was adjusted in different experiments so the arrival of the backlighter protons at the foil would occur with different delays after the laser interaction beam was turned on. A metal mesh was placed between the backlighter and the foil to divide the protons into beamlets.

Critical to these experiments are the unique properties of the backlighter: it is *pulsed*, truly *monoenergetic*, and *isotropic*. It is used with imaging detectors (CR-39) that are matched to each type of proton, detect individual protons, and provide information about the energy of each proton [12,21]. Monoenergetic protons provide an unambiguous relationship between the measured lateral deflection of proton beamlets and the strength of any B fields through which they travel. An isotropic backlighter allows images of a large area to be made without variations in proton energy or fluence over the field of view; it also makes possible multiple experiments at different angles around the backlighter (Fig. 1). Interactions of separate laser-produced bubbles and their B fields are illustrated in the face-on images of Figs. 2(a) and 2(b) for four and two laser beams, respectively. Figure 2(a) shows images recorded during 7 shots in which laser timing was adjusted so protons arrived at the foil at designated times after the interaction beams were turned on. The experiments covered the periods when the beams were on (0.3 to 1 ns) and off (1.2 to 2.4 ns). Figure 2(b) shows similar data for two beams. The 4-beam and 2-beam experiments differed by having 1.8-mm and 1.4-mm beam spacing (center-to-center), respectively, and by having different angles of incidence on the foil (23° from the normal in the 4-beam cases and 47.8° in the 2-beam cases); the 2-beam illumination was therefore more elliptical (axis ratio ~1.5).

Figure 3 shows 2D simulated spatial distributions of n_e, T_e, and $|B|$ in a plane perpendicular to the foil at times 0.6 and 1.5 ns (the latter 0.5 ns after the 1-ns laser beam turns off). The laser is assumed incident from the right and the imaging protons incident from the left. Figures 3(c1) and 3(c2) show that MG B fields are localized on the surface of the bubble (as recently verified experimentally [13]). In this case the trajectories would be deflected toward increas-

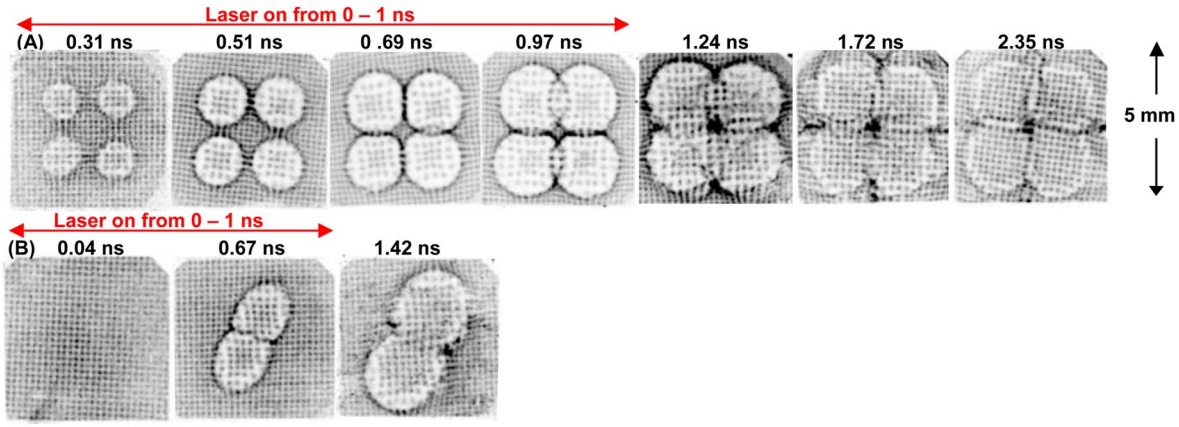

FIG. 2 (color online). Radiographs generated when four (A) or two (B) laser beams were incident on a CH foil. In (A), interbubble interactions were minimal while the laser was on (<1 ns) but significant later. At 1.24 and 1.72 ns, asymmetric bubble structure [18] is superposed on a static background pattern that is still visible at 2.35 ns, after most of the bubble structure has dissipated; the pattern is from fields around the burn-through hole (Fig. 3). In (B), the bubbles have interacted and reconnection has occurred by 0.67 ns. By 1.42 ns, most fields in the intersection region have reconnected (remaining distortion is largely due to burn-through holes).

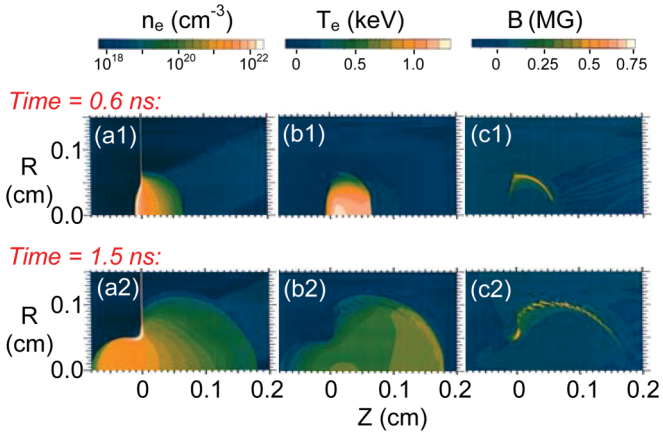

FIG. 3 (color). Distributions of n_e, T_e, and B-field amplitude in an isolated plasma bubble generated by a laser beam incident from the right, simulated with the 2D code LASNEX [24]. The laser beam is equivalent to each beam in the 4-beam experiment. The foil is at $Z = 0$. The field is perpendicular to the image plane. While the laser is on, the B field is localized on the surface of the quasihemispherical bubble (c1). A strong field structure appears at the edge of the hole burned into the foil some time after the laser is off (c2).

ing radius (R). The net effect in recorded images is a magnification of the bubble, with larger beamlet spacing inside the bubble than outside. Each bubble seen in the images of Figs. 2(a) and 2(b) has an apparent border where beamlets pile up to form a sharp circular ring, but because of magnification the touching or overlapping of different beamlet-pileup circles in the images from ~0.5 to 1 ns do not always indicate that the plasma bubbles and field structures have interacted or even touched yet (see Fig. 4).

The displacement $\boldsymbol{\xi}$ of each individual beamlet, projected from detector plane back to the foil, relative to the position it would have if there were no fields, is

$$\boldsymbol{\xi} = -\frac{qa(A-a)}{Am_p v_p}\int \mathbf{B}\times d\boldsymbol{l}, \tag{1}$$

where q, m_p, and v_p are the proton charge, mass, and velocity, respectively; a and A are the geometric parameters shown in Fig. 1; and $d\boldsymbol{l}$ is the differential path length along the proton trajectory.

Sample analyses are shown in Fig. 4 for two images from Fig. 2. Figure 4(a1) represents a time (0.69 ns) in the 4-beam case before the bubbles grew large enough to touch each other, although the fields have the effect of magnifying the bubble images and making them appear to overlap in the image. Figure 4(b1) shows the measured $\boldsymbol{\xi}$ for each beamlet, and Fig. 4(c1) shows the field map (spatial distribution of $|\int \mathbf{B}\times d\boldsymbol{l}|$) at the location of the foil. Figure 4(d1) shows a lineout through the field map, illustrating the localization of the field on the outside of the bubble; fields from the two bubbles do not yet touch each other. Figure. 4(a2) represents a similar time in the 2-beam case. Because of the closer spacing and the elliptical laser footprint described above, the bubbles in this case have collided, as illustrated in Figs. 4(b2) and 4(c2). The field map [Fig. 4(c2)] and the lineout [Fig. 4(d2)] show that the field energy density is substantially smaller in the region of intersection of the two bubbles than in the other regions around the peripheries of the bubbles, indicating that reconnection has occurred. [Quantitative analysis of the bubble overlap, after the laser is off, is complicated due to the interference of the burn-through hole [Fig. 3(c2)] and the growth of instabilities [18].]

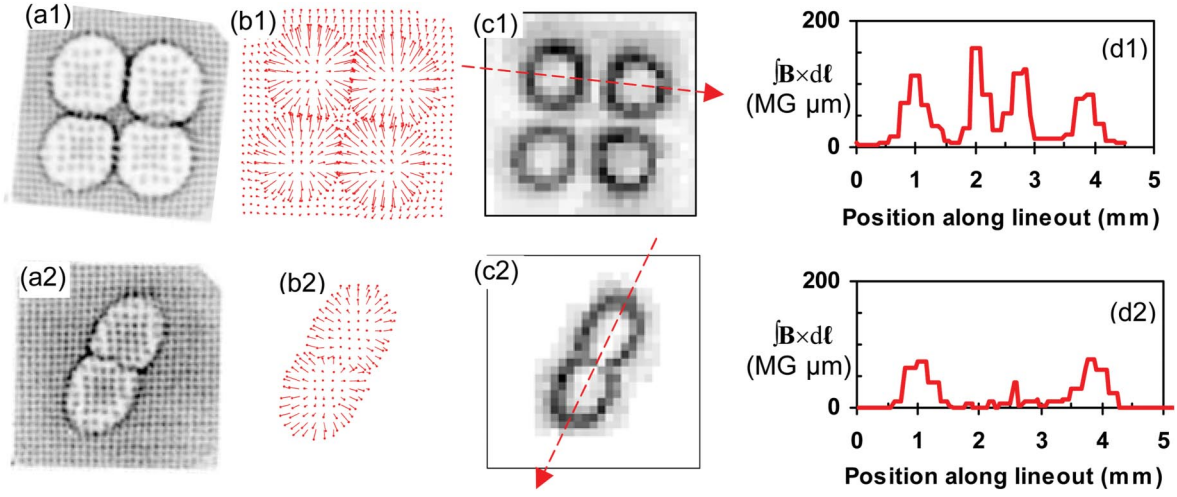

FIG. 4 (color). Radiography images were used to deduce maps of the B field at the foil. In (a1),(a2), from Figs. 2(a) and 2(b), the location of each beamlet can be compared with the location it would have had with no B fields (beamlets on the image edges define the grid of "undeflected" locations); (b1),(b2) show displacement vectors ξ. Arrays of displacement amplitudes are shown as images [(c1),(c2)]; each pixel represents one beamlet, with value proportional to displacement. Displacement is proportional to $\int \mathbf{B}\times d\boldsymbol{l}$ along the particle trajectory, so lineouts of (c1),(c2) (along the red arrows) provide quantitative measurements of $|\int \mathbf{B}\times d\boldsymbol{l}|$ at the foil location [(d1),(d2)].

To place these measurements in the broader context of basic plasma physics, we can calculate the magnetic Reynolds number

$$R_m = \frac{L_\perp v}{D_m} \approx \frac{\nabla \times (\mathbf{v} \times \mathbf{B})}{\nabla \times (D_m \nabla \times \mathbf{B})}, \quad (2)$$

where $L_\perp \approx T_e/\nabla T_e \sim 50$–$100$ μm is a length scale characteristic of the thickness of the field layer on the surface of the bubble [18]. When the laser is on, $R_m \sim 1000$ (v is the bubble expansion velocity $\sim 5 \times 10^7$ cm s^{-1} and diffusion $D_m \sim 4 \times 10^2$ cm^2 s^{-1}), so the fields must be frozen in and move with the plasma. And because of the high value of β ($\gg 1$), the plasma flow is not significantly affected by the fields despite their MG levels. The bubble expansion in this regime can be approximately described as "free streaming," because the velocity is of the order of the ion sound velocity ($C_s \sim 2 \times 10^7$ cm s^{-1}).

Returning to germane results in the 4-beam data, there is little or no interaction between field structures localized to different bubble surfaces at the earliest times [Figs. 4(c1) and 4(d1)]. Integrals under the individual peaks in Fig. 4(d1) are approximately equal [$\sim(5.0 \pm 0.5) \times 10^4$ MG μm^2], indicating little if any field cancellation. The field lines retain their original topology of closed loops around each beam spot. Eventually, the separate bubbles touch each other; fields with opposing directions mix and cancel. The sharp gradients of n_e and T_e at the individual bubble edges (Fig. 3) must diminish as the bubbles coalesce, removing the principal field-generating mechanism ($\nabla n_e \times \nabla T_e$). This field reconnection is evident in the field map of Fig. 4(c2), which shows diminished fields at the point of bubble intersection, and in the lineout of Fig. 4(d2). Integrals under the lineout portions representing the walls of the bubbles are $\sim 4 \times 10^4$ MG μm^2 for each outer wall and $\sim 4 \times 10^3$ MG μm^2 for the two overlapping walls; this indicates at least a 95% reduction in $|\int \mathbf{B} \times d\mathbf{l}|$ in the intersection region. Based on these measurements and the observed scale sizes of the bubble, the field energy converted to plasma internal energy in the reconnection region was $\sim 2.5 \times 10^2$ J cm^{-3}. Taking n_e around the bubble edge to be $\sim$1%–10% of the critical density ($n_c \sim 10^{22}$ cm^{-3}), we estimate a resulting rise in plasma temperature of 1–10 eV, a small and presently immeasurable fraction ($\leq 1\%$) of T_e (~ 1 keV). This is expected for our high-β plasma; reconnection energy has little direct impact on the dynamics of the interacting bubbles. However, the change in topology, as mediated through the reconnection, will certainly affect particle and heat transport and structural evolution.

To further illuminate reconnection in this high-β, HED experiment, the data can, very qualitatively, be compared to predictions of the standard Sweet-Parker (SP) model [22,23] of resistive reconnection (SP is restricted to 2D and steady state, neither of which exist in this experiment.) The experimental time scale for reconnection can be estimated as $\tau_{R,E} \sim 0.2$ ns by dividing the apparent width of the field layer at the surface of the bubble in Fig. 4(c1) by twice the bubble expansion velocity. In contrast, the SP reconnection time is $\tau_{R,\mathrm{SP}} = (\tau_D \tau_A)^{1/2} \sim 5$ ns, where $\tau_D = 0.5 L_\perp{}^2 D_m{}^{-1} \sim 30$ ns is the B-field diffusion time, $\tau_A = L_\perp v_A{}^{-1} \sim 1$ ns is the Alfvén transit time across the field layer, and $V_A \sim 5 \times 10^6$ cm s^{-1} (taking $n_i \sim 1 \times 10^{20}$ cm^{-3} and inferring, from Fig. 4 and earlier results [13], that $B \sim 0.5$ MG for a proton path length ~ 200 μm). Though there are uncertainties in the estimates of these parameters, the comparison suggests that the reconnection illustrated in Figs. 4(a2), 4(b2), 4(c2), and 4(d2) is dominated by plasma hydrodynamics. To this point, and to the best of knowledge, unlike all other reconnection experiments, the reconnection time is smaller than even the Alfvén time. Comparison beyond this, due to the 3D character of these experiments, requires the development of a 3D reconnection model.

The work described here was performed in part at the LLE National Laser User's Facility (NLUF), and was supported in part by U.S. DOE (Grant No. DE-FG03-03SF22691), LLNL (subcontract Grant No. B504974), and LLE (subcontract Grant No. 412160-001G).

[1] D. Biskamp, *Magnetic Reconnection in Plasmas* (Cambridge University Press, Cambridge, U.K., 2000).
[2] S. Masuda *et al.*, Nature (London) **371**, 495 (1994).
[3] T. D. Phan *et al.*, Nature (London) **439**, 175 (2006).
[4] J. B. Taylor, Rev. Mod. Phys. **58**, 741 (1986).
[5] J. Nuckolls *et al.*, Nature (London) **239**, 139 (1972).
[6] M. A. Yates *et al.*, Phys. Rev. Lett. **49**, 1702 (1982).
[7] R. C. Davidson, *Frontiers in High Energy Density Physics* (National Academies Press, Washington, DC, 2003).
[8] R. P. Drake, *High-Energy-Density Physics* (Springer Press, New York, 2006).
[9] J. A. Stamper *et al.*, Phys. Rev. Lett. **26**, 1012 (1971).
[10] D. G. Colombant, Phys. Rev. Lett. **38**, 697 (1977).
[11] B. A. Remington *et al.*, Science **284**, 1488 (1999).
[12] C. K. Li *et al.*, Rev. Sci. Instrum. **77**, 10E725 (2006).
[13] C. K. Li *et al.*, Phys. Rev. Lett. **97**, 135003 (2006).
[14] A. Mackinnon *et al.*, Rev. Sci. Instrum. **75**, 3531 (2004).
[15] P. Nilson *et al.*, Phys. Rev. Lett. **97**, 255001 (2006).
[16] S. I. Braginskii, *Review of Plasma Physics 1* (Consultants Bureau, New York, 1965).
[17] M. G. Haines, Phys. Rev. Lett. **78**, 254 (1997).
[18] C. K. Li *et al.*, Phys. Rev. Lett. **99**, 015001 (2007).
[19] T. R. Boehly *et al.*, Opt. Commun. **133**, 495 (1997).
[20] T. J. Kessler *et al.*, in *Laser Coherence Control: Technology and Applications*, Proc. SPIE Int. Soc. Opt. Eng. (SPIE-International Society for Optical Engineering, Bellingham, WA 1993).
[21] F. Séguin *et al.*, Rev. Sci. Instrum. **75**, 3520 (2004).
[22] P. A. Sweet, Nuovo Cimento Suppl. **8**, 188 (1958).
[23] E. N. Parker, Astrophys. J. Suppl. Ser. **8**, 177 (1963).
[24] G. B. Zimmerman *et al.*, Comments Plasma Phys. Control. Fusion **2**, 51 (1975).